Preflight Calibration of the Chinese Environmental Trace Gases Monitoring Instrument (EMI)

MinJie Zhao, FuQi Si, HaiJin Zhou, ShiMei Wang, Yu Jiang, WenQing Liu

Key Laboratory of Environmental Optics and Technology, Anhui Institute of Optics and Fine Mechanics, Chinese Academy of Sciences, Hefei 230031, China

Correspondence to: FuQi Si (sifuqi@aiofm.ac.cn)

Abstract

An Environmental trace gases Monitoring Instrument (EMI) is a nadir-viewing wide-field imaging spectrometer, which aims to quantify the global distribution of tropospheric and stratospheric trace gases, and is planned to be launched in 2018.05.09. The selected wavelength bands for EMI are ultraviolet channels: UV1 (240–315 nm), UV2 (311–403 nm) and visible channels: VIS1 (401–550 nm), and VIS2 (545–710 nm). The spectral resolution is 0.3–0.5 nm, and the swath is approximately 114 ° wide to achieve a one-day global coverage. The preflight calibration of the EMI is discussed in this paper. Tunable laser and rotating platform are adopted for an EMI wavelength calibration of the entire field of view. The accuracy of the wavelength calibration is less than 0.05 nm. In addition, the solar calibration mode shows the same results compared with Earth observation mode. A thermal vacuum test is performed to investigate the influence of in-orbit thermal vacuum conditions on the EMI, and EMI spectral response changes with pressure, optical bench temperature, and charge-coupled device (CCD) detector temperature are obtained. For a radiometric calibration of UV1, a diffuser plate with a 1000 W xenon lamp, which produces a sufficient UV output, is selected. An integrating sphere system with tungsten halogen lamp is selected for the UV2, VIS1, and VIS2. The accuracies of radiance calibration are 4.53% (UV1), 4.52% (UV2), 4.31% (VIS1), and 4.30% (VIS2). The goniometry correction factor and irradiance response coefficient of the EMI are also calibrated on the ground for an in-orbit calibration of the solar. A signal-to-noise ratio (SNR) model of the EMI is introduced, and the EMI in-orbit SNR is estimated using the SNR and MODTRAN radiance models.

1 Introduction

Numerous space-borne spectrometers, such as GOME [*JOHN P. BURROWS et al., 1999*], SCIAMACHY [*H. BOVENSMANN et al., 1999*], GOME-2 [*Rosemary Munro et al., 2016*], and OMI [*Pieternel F. Levelt et al., 2006*], have been successfully applied to the global monitoring of atmospheric trace gas distributions. These instruments measure sun radiance backscattered from the Earth's atmosphere in the UV-VIS wavelength range. TROPOMI builds upon the heritages of SCIAMACHY and OMI instruments, which were

launched in 2017 on ESA's Sentinel 5 precursor satellite [*Rovert Voors et al., 2012*].

An Environmental trace gases Monitoring Instrument (EMI) is a space-borne nadir-viewing wide-field imaging spectrometer, which is used to obtain global distributions of tropospheric and stratospheric trace gases (e.g., NO2, O3, HCHO, and SO2) at high spatial and spectral resolution. The EMI is planned to be launched in 2018.05.09.

Performance requirements

Spectral range: UV1:240–315 nm; UV2:311–403 nm; VIS1:401–550 nm; VIS2: 545–710 nm;

Spectral resolution: <0.5 nm;

Accuracy of the on-ground wavelength calibration: <0.05 nm;

Accuracy of the on-ground radiometric calibration: <5%;

SNR:

UV channel: >200 (@1.27 $\mu W / cm^2 / sr / nm$)

VIS channel: >1300 (@10.89 $\mu W / cm^2 / sr / nm$)

Instrument description

The EMI has four spectral channels (i.e., UV1, UV2, VIS1, and VIS2) that range from 240 nm to 710 nm. Each channel adopts an Offner imaging spectrometer and 2D charge-coupled device detectors. The EMI enables an instantaneous field of view (FOV) of 114° (corresponding to a 2600 km broad swath on the Earth's surface), and the space resolution is either 8 km/12 km (UV/VIS channel) or 48 km (UV and VIS channels) at nadir, depending on an electronic binning factor (Table 1). Moreover, a one-day global coverage can be realized. The anticipated lifetime of the EMI is 8 years, and its properties are listed in Table 1.

Table 1. EMI instrument properties

Spectral sampling	UV1: 0.08 nm; UV2: 0.09 nm
	VIS1: 0.12 nm; VIS2: 0.13 nm
Spectral resolution	0.3–0.5 nm
Telescope swath IFOV	114 °(2600 km on the ground)
Telescope flight IFOV	0.5 °(6.5 km on the ground)
CCD detectors	UV: 1072×1032 (spectral $\times$ spatial) pixels
	VIS: 1286×576 (spectral $\times$ spatial) pixels
Ground pixel size at the nadir	13 km $\times$ 48 km (electronic binning factor
	UV: 24, VIS: 16)
	13 km $\times$ 8 km (UV, binning factor 4)
	13 km $\times$ 12 km (VIS, binning factor 4)
Orbit	Polar, sun-synchronous; Orbit period: 98 min, 53 s; Ascending node equator crossing time: 13:30

55   The optical layout of the EMI is illustrated in Fig. 1. The EMI consists of a telescope and four spectrometers.

The telescope provides an instantaneous FOV of 114 ° in the swath direction and 0.5 ° in the flight direction, thereby yielding an overall ground coverage of approximately 2600 km × 6.5 km at an altitude of 705 km. The spatial resolution in the swath and flight directions depend on the electronic
60   binning factor and CCD integration time, respectively. Four Offner imaging spectrometers are adopted by the EMI, where each spectrometer has a convex grating and a 2D CCD detectors. The Offner imaging spectrometer can be easily miniaturized and is lightweight and suitable for the development of space technology. This spectrometer is also suitable for high spatial and spectral resolution detection systems. The EMI covers a 240–710 nm range with a spectral resolution of 0.3–0.5 nm.
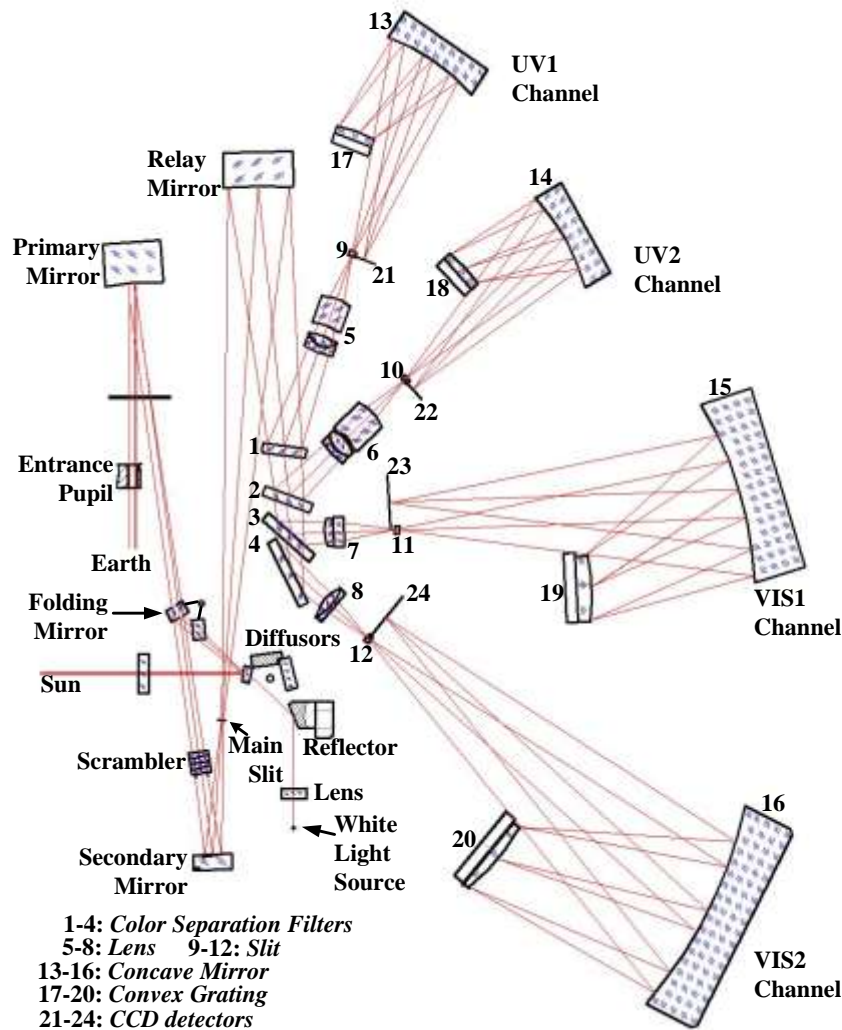
Fig.1. Optical layout of the EMI

One observation mode and two calibration modes are included in the EMI. The observation mode is used to detect atmospheric scattering light, and the two calibration modes are utilized for in-orbit calibration.

In the observation mode, the Earth radiance enters the telescope through the entrance pupil and is imaged on the main slit after reflection by the primary and secondary mirrors. A polarization scrambler is located before the secondary mirror, which is used to enable the EMI to be insensitive to the polarization state of the incident light. Furthermore, a relay mirror behind the main slit reflects the incident light on Color separation filters 1–4. Color separation filter 1 reflects the 240–315 nm range of the spectrum to the UV1 channel and transmits the rest of the spectra to Color separation filter 2.

Consequently, 311–403, 401–550, and 545–710 nm ranges of the spectra are reflected to the UV2, VIS1, and VIS2 channels by Filters 2–4. The spectrum from the filters is imaged on Spectrometer slits 9–12 (10 mm × 60 μm) through Lenses 5–8. Final dispersion is achieved by Convex grating 17–20 after reflection by Concave mirrors 13–16, which are used in the first order. The spectrum is imaged onto 2D (spectral and spatial dimensions) CCD detectors 21–24.

The first calibration mode is solar calibration. The solar spectrum that is observed by this mode is used to perform accurate wavelength calibrations and normalize the Earth spectra to obtain absolute Earth reflectance spectra. Solar radiation enters the instrument through a mesh (transmission 10%) by opening the solar aperture mechanism and is diffused by a selected diffuser. Light from the diffusers illuminates the folding mirror and is then reflected to a telescope optical path. The folding mirror in this position blocks the Earth radiance from the primary mirror. The EMI equipped with one surface reflectance aluminum diffuser (40 mm × 16 mm) and one quartz volume diffuser (QVD; 40 mm × 16 mm × 6 mm), which consists of a 6 mm thick quartz ground on both sides and is coated with aluminum on the backside. In addition to its use for radiometric calibration, the QVD is used once per day to provide a solar reference spectrum because considerably less structures are introduced by the QVD than the aluminum diffuser [*Ruud Dirksen et al., 2004, Johan de Vries et al., 2005*]. The aluminum diffuser is mainly used for monitoring optical degradation behavior in space. This monitoring is performed monthly.

The second calibration mode is the white light source (WLS) calibration. A quartz tungsten halogen WLS (6 V, 10 W) is used to monitor CCD detector properties. The light from the WLS travels through the transmission diffuser and is reflected to the telescope optical path.

Large spectral range from 240 nm to 710 nm combined with high spectral resolution(0.3 nm to 0.5 nm) of the EMI enables the measurement of several trace gases(e.g., NO2, O3, SO2, BrO, HCHO) as well as aerosol, see Table 2. To achieve a high retrieval precision, a high SNR is required for the scattered radiance from the UV to the VIS.

Table 2. EMI data products.

Product Name	Wavelength Band/nm
O3	300-345(UV1,UV2)
SO2	305-330(UV1,UV2)
NO2	425-500(VIS1)
BrO	344-360(UV2)
HCHO	335-360(UV2)
Aerosol	UV2,VIS1,VIS2

2 Preflight calibration

The EMI detection capability must match the changes in the Earth radiance. Thus, the instrument can

obtain enhanced measurements from in-orbit. High-accuracy spectral and radiometric calibrations are required on the ground to obtain the response performance of the instrument [*A. Perez Albinana et al., 2002, Marcel Dobber et al., 2006, B. Ording et al., 2016, Quintus Kleipool et al., 2018*].

2.1 Spectral calibration

A spectral calibration is performed in Earth observation mode (EOM) during laboratory calibration. The calibration results of the EOM can be applied to solar calibration mode (SCM) (see Section 2.3). The utilized tunable laser (OPOTEK: RADIANT) exhibits output spectrum ranges of 193–410 and 410–2500 nm, which can cover 240–710 nm of the EMI with the wavelength accuracy of 10 pm. In addition, the spectral calibration is performed in a clean room, thereby reducing the influence of temperature and humidity.

The spectral calibration is required in the spectral and spatial dimensions. The tunable laser output wavelength space is 5 nm for the UV2 channel and 10 nm for the UV1, VIS1, and VIS2 channels in the spectral dimension. The spectral lines have full widths at half maximum (FWHM) that are typically 1 order of magnitude lower than the EMI spectral resolution, thus providing delta inputs to the EMI in the wavelength dimension. Therefore, the influence of the slit function of the laser is removed. In the spatial dimension, the instrument must be rotated for 21 steps in accordance with the 5.5 ° interval to cover the full FOV. The spectral calibration and dark background are recoded.

The wavelength calibration of the EMI instrument is expressed as

$$\lambda_{i,j} = \sum_{m=0}^{N} c_{k,j} \cdot p^k ,\qquad(1)$$

where λ is the wavelength of a pixel, i is the column number, j is the row number, and $c_{m,j}$ is the wavelength calibration polynomial coefficient. N is the order of the polynomial, which is 3 for the EMI wavelength calibration. The spectral lines of a laser distribute uniformly in the spectral dimension, thereby ensuring a polynomial fitting precision. The four channel wavelength calibrations of a center FOV (CFOV) in the spectral dimension are depicted in Fig. 2.
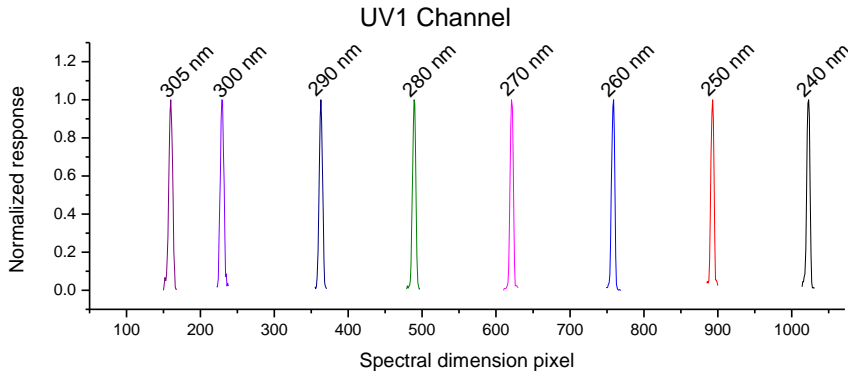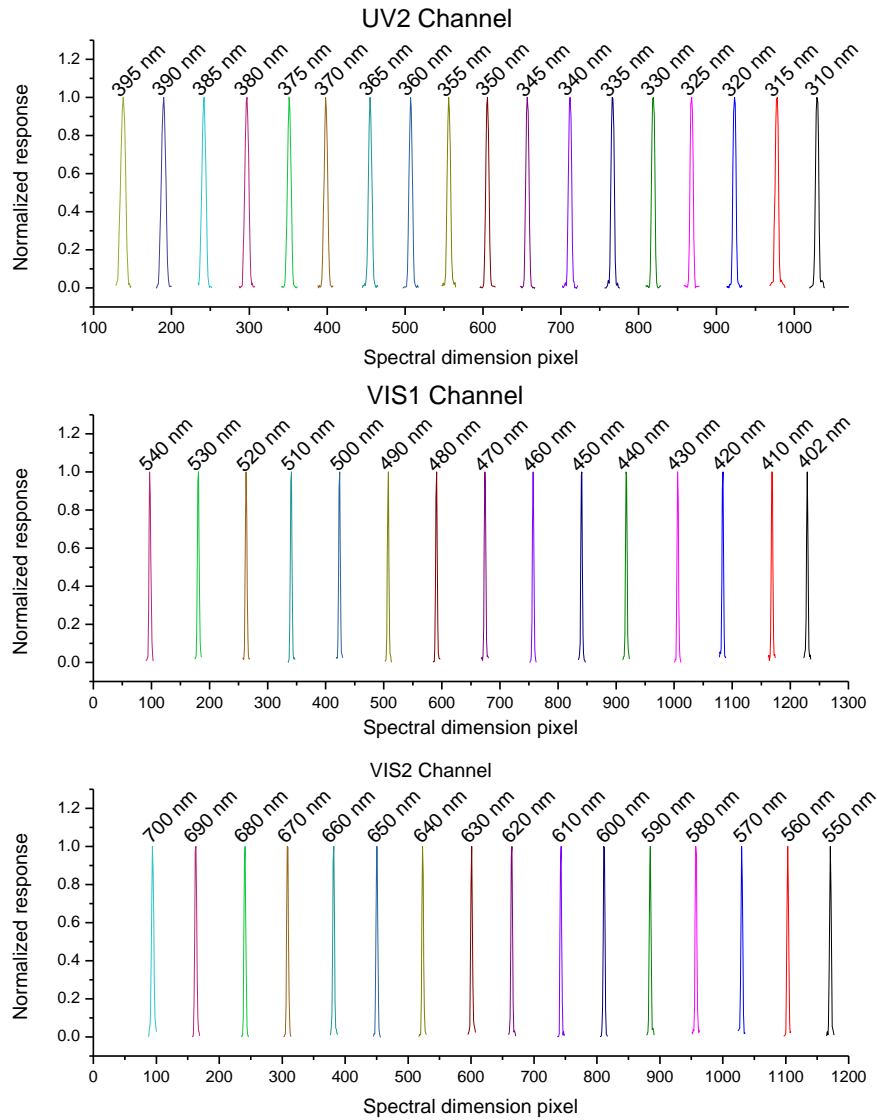
Fig.2. EMI CFOV wavelength calibration for each channel. The upper panel presents the UV channel, whereas the lower panel displays the VIS channel. The spectral responses are normalized.

The CFOV spectral ranges of each channel are summarized in Table 3. The spectral range in other FOVs is discussed subsequently.

Table 3. CFOV spectral ranges

Channel	Spectral Range/nm
UV1	236.44–317.28
UV2	306.08–407.12
VIS1	395.50–552.63
VIS2	534.63–712.90

The spectral calibration in the spatial dimension is demonstrated in Fig. 3. A smile effect in the spatial dimension exists in each channel, and the wavelength position on a detector array varies with different FOVs [*P. S. Barry et al., 2002, Robert A et al., 2003, Luis Guanter et al., 2006*]. The wavelength in a marginal FOV shifts to a long wave for the UV channel and to a short wave for the VIS channel. Figure 3 exhibits the wavelength (pixel) shifts between the CFOV and the other FOVs.
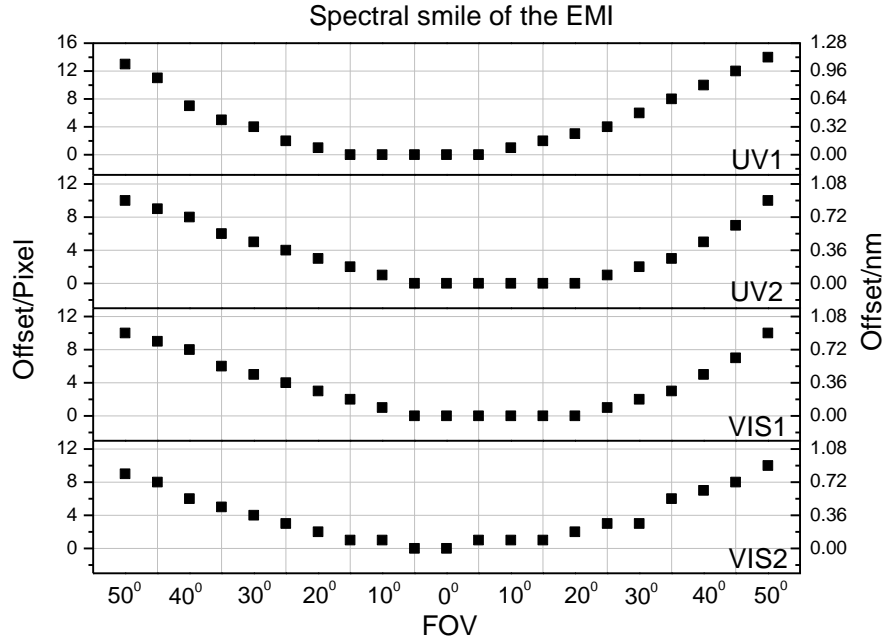
Fig.3. Spectral calibration in the spatial dimension.

The wavelength (pixel) shift enlarges from the CFOV to the edge FOV. The UV1, UV2, VIS1, and VIS2 wavelength (pixel) shifts of the edge FOV are 1.12 nm (14 pixels), 0.9 nm (10 pixels), 1.2 nm (10 pixels), and 1.3 nm (10 pixels), correspondingly. For the L1b processor of the EMI, the spectral smile effect will be calibrated using a spectrum-matching technique.

The spectral response of the EMI can be considered as a Gaussian-type function. The FWHM of an instrumental line shape (ILS) function is known as the spectral resolution of the spectrometer channels. The FWHM of the ILS by Gaussian fitting is displayed in Table 4.

Table 4. FWHM of the ILS

FOV	UV1/nm	UV2/nm	VIS1/nm	VIS2/nm
50 °	0.44	0.45	0.34	0.49
40 °	0.39	0.39	0.29	0.39
30 °	0.40	0.38	0.29	0.40
20 °	0.42	0.43	0.31	0.39
10 °	0.42	0.47	0.33	0.39
0 °	0.43	0.49	0.34	0.40
10 °	0.41	0.46	0.34	0.38
20 °	0.38	0.41	0.32	0.34
30 °	0.36	0.36	0.34	0.30
40 °	0.38	0.36	0.38	0.28
50 °	0.45	0.43	0.48	0.34

155   The overall accuracy of the spectral calibration is determined by three major factors as follows: (1) the accuracy of a laser output wavelength, which is less than 0.01 nm; (2) the accuracy of the EMI spectral response, which is determined by 20 spectral response measurements from the same laser output line (<0.014 nm); (3) a fitting method (using least squares method). The accuracy of the polynomial fitting is approximately 0.040 nm, and the Gaussian fitting is approximately 0.020 nm. The
160   final accuracy of the wavelength calibration is less than 0.05 nm, and the accuracy FWHM of the ILS is less than 0.03 nm.

2.2 Thermal vacuum test

The spectral calibration discussed previously is performed in an atmospheric environment, which can provide detailed spectral response characteristics. A thermal vacuum test is performed (Fig. 4) to
165   determine the difference between the atmospheric and vacuum environments and obtain the spectral response characteristics under thermal vacuum conditions (EMI in-flight conditions). A mercury argon lamp is used as light source for EMI. The EMI views a mercury argon lamp through a thermal vacuum chamber window. Owing to the limitations of the rotational device and window size, the EMI CFOV is measured in the thermal vacuum chamber.
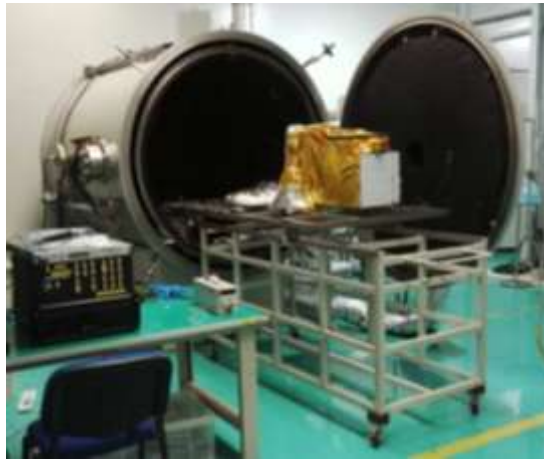
Fig.4. Thermal vacuum test of the EMI.

The thermal vacuum conditions include pressure, optical bench temperature, and CCD temperature.

Pressure:

AE: Atmospheric Environment

PV: Pumping Vacuum

NFP: Nitrogen Filling Process

Optical bench temperature

LT: Low Temperature (276 K)

HT1: High Temperature 1 (290 K)

HT2: High Temperature 2 (288 K)

HT3: High Temperature 3 (299 K)

MT1: Middle Temperature 1 (284K)

MT2: Middle Temperature 2 (283K)

MT3: Middle Temperature 3 (285K)

NTC: No Temperature control

CCD temperature:

UV1, UV2: 254 K

VIS1, VIS2: The temperature is the same as that of the optical bench.

The wavelength shift and FWHM of the ILS in different conditions are analyzed.

The pixel position that corresponds to the emission peak of the mercury argon lamp is obtained by Gaussian fitting. The wavelength shifts of the four channels are displayed in Fig. 5.
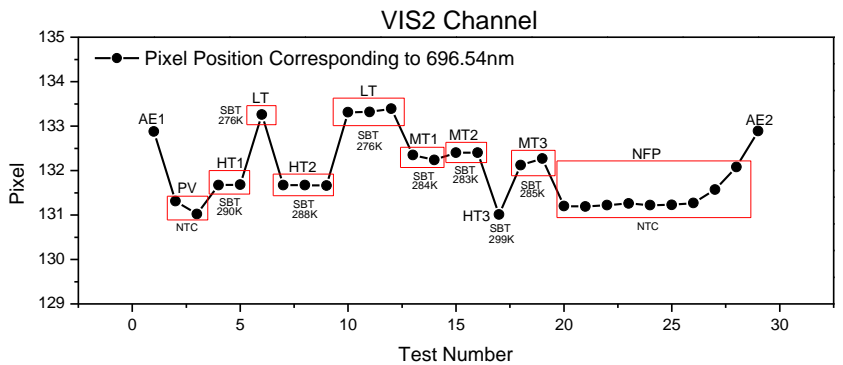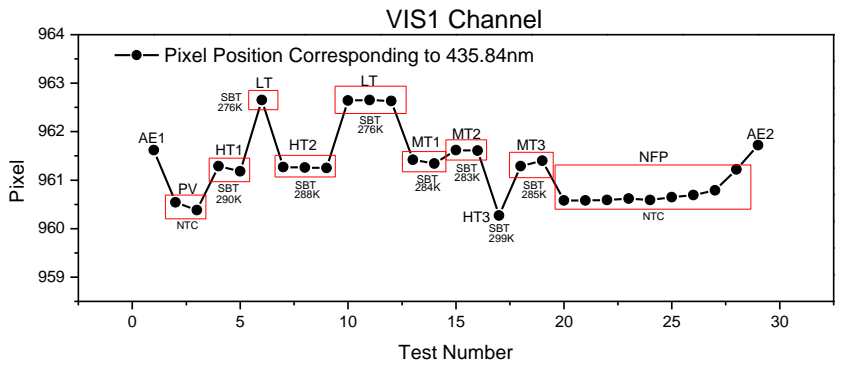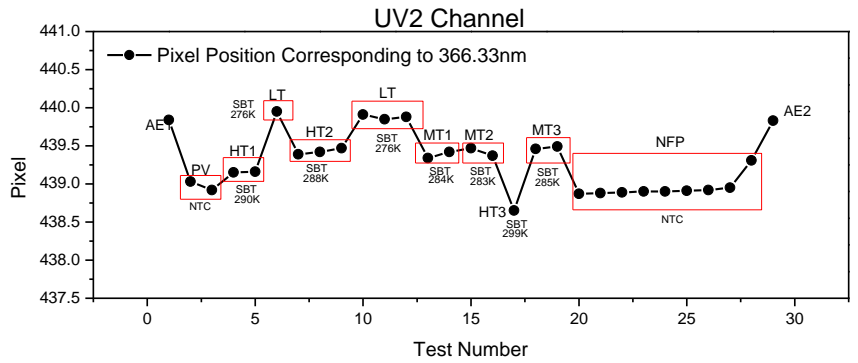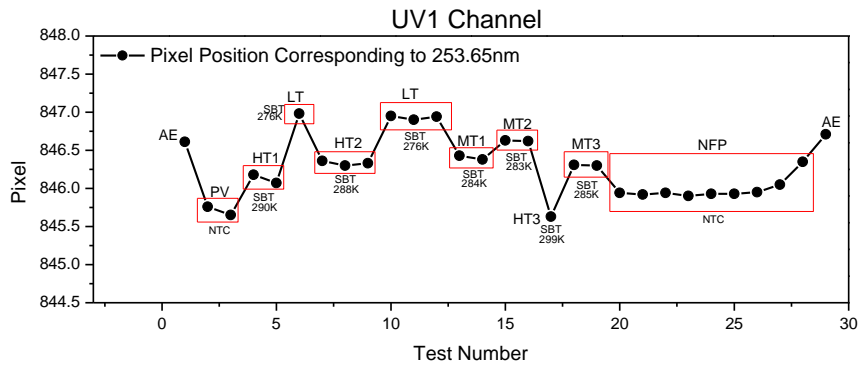
195

Fig.5. Wavelength shifts from the atmospheric environment to vacuum: UV1/0.8 pixel (approximately 0.06 nm), UV2/0.8 pixel (approximately 0.07 nm), VIS1/1 pixel (approximately 0.1 nm), VIS2/1.5 pixel (approximately 0.2 nm); Wavelength shifts from HT1 to LT in vacuum: UV1/1 pixel (approximately 0.1 nm), UV2/1 pixel (approximately 0.1 nm), VIS1/1.5 pixel (approximately 0.2 nm), VIS2/1.5 pixel (approximately 0.2 nm)

The wavelength shifts $\Delta\lambda$ are determined by

$$\Delta\lambda = \lambda_{Vac} - \lambda_{At} = (1 - 1/n)\lambda_{Vac}, \tag{2}$$

where λ_{Vac} and λ_{At} are the wavelengths in the thermal vacuum chamber and atmospheric environment. The atmospheric refractivity $n > 1$ because the thermal vacuum chamber pressure is lower than the atmospheric pressure. The wavelength shifts to a long wave with the decrease in pressure (n becomes large) and to short wave with the increase in pressure (n becomes small) in the thermal vacuum chamber (see PV and NFP results). Furthermore, the wavelength shifts enlarge with the increase in λ_{Vac}. The results show that the shifts are 0.06 nm for 253.625 nm and 0.2 nm for 696.54 nm.

These results also indicate that the wavelength shifts change with the optical bench temperature under a vacuum condition. The wavelength shifts to a long wave with the increase in the optical bench temperature and to a short wave with the decrease in the optical bench temperature. The wavelength shift is approximately 0.1 nm for UV1 and UV2 and is approximately 0.2 nm for VIS1 and VIS2.

The FWHM of the ILS of four channels are presented in Fig. 6.
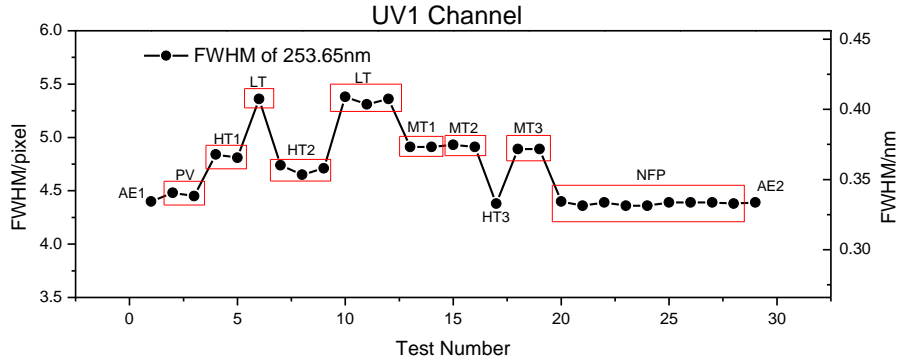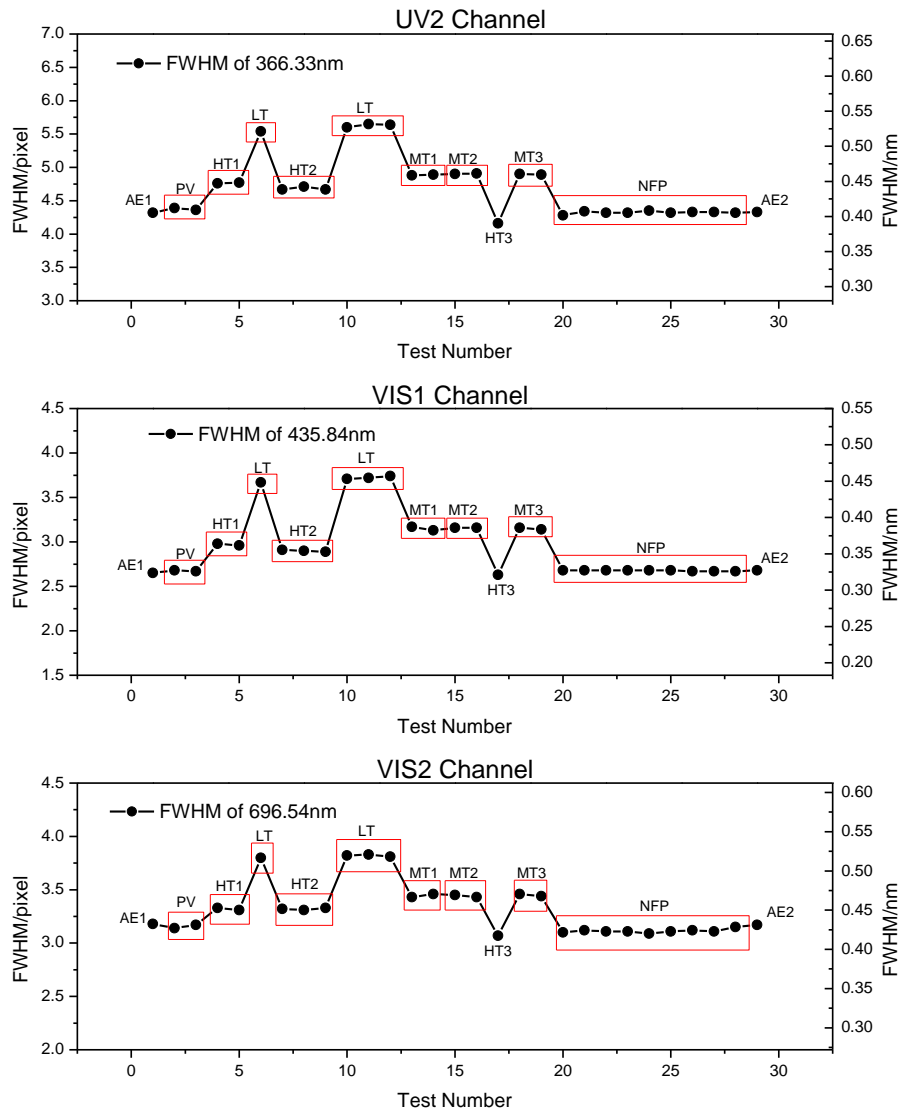
Fig.6. Results of the thermal vacuum test on the FWHM of the ILS. The results show that (1) the FWHM of the ILS is essentially the same in different pressures in the thermal vacuum chamber (see AE, PV, and NFP results); (2) the FWHM of the ILS shrinks with the increase in the optical bench temperature under a vacuum condition.

The FWHM of the ILS changes with the optical bench temperature (Table 5).

Table 5. FWHM of the ILS changes with optical bench temperature

FWHM of the ILS	Optical bench temperature/K						
	276	283	284	285	288	290	299
UV1/nm	0.41	0.37	0.37	0.37	0.36	0.36	0.33
UV2/nm	0.52	0.46	0.46	0.46	0.45	0.45	0.39
VIS1/nm	0.45	0.39	0.39	0.39	0.36	0.36	0.32
VIS2/nm	0.52	0.47	0.47	0.47	0.45	0.45	0.42

In Table 5, the optical bench temperature significantly influences the spectral resolution of the EMI. For example, the relative deviation of the spectral resolution between the optical bench temperatures of 276 and 299 K is up to 25%. Therefore, the in-orbit optical bench temperature of the EMI can be set up in accordance with the FWHM of the ILS results of the thermal vacuum test.

2.3 Spectral calibration in the solar calibration mode

The spectral calibration in the EOM is introduced previously. The calibration in the SCM shows that the same results are obtained compared with the EOM. We also obtain the solar spectrum from both modes on the ground. An optical fiber and a small telescope are used to introduce direct sunlight to the Earth and solar ports. The solar spectrum at the CFOV of the EMI (except UV1 because the wavelength range in this channel is not visible on the ground) is illustrated in Fig. 7.
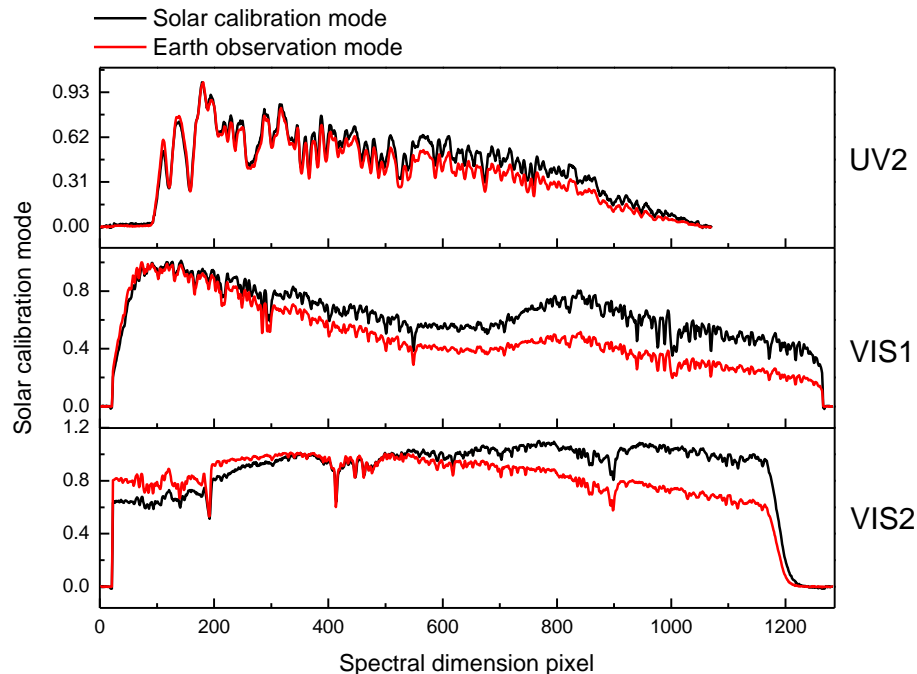
Fig.7. Solar spectrum obtained by the EMI on the ground. The aluminum diffuser is used to observe

240 the solar spectrum in the SCM (Fig. 1).

In Fig. 7, the pixel corresponds to the same wavelength in the two modes. The difference between the spectral shapes is due to the aluminum diffuser's spectral characteristics, such as hemispheric reflectance and bidirectional reflectance distribution function [*F. E. Nicodemus et al., 1977, Kenneth J. Voss et al., 2000, Xuemin Jin et al., 2009*]. In addition, the spectral features of the aluminum diffuser are introduced
245 to the solar spectrum. The irradiance calibration of the sun through a space-borne diffuser is discussed subsequently.

3 Radiometric calibration

Radiometric calibration is performed in the EOM and SCM on the ground. Several operating parameters, such as three integration times (i.e., 0.5, 1, and 2 s) and 64 gain steps (i.e., 0–63 with an interval of 1),
250 are designed for the EMI to fulfill the requirements of an in-orbit observation. The radiometric calibration is performed at different integration times, and the relationship between gain steps and gain values is measured.

3.1 Radiometric calibration system

Integrating sphere and diffuser plate radiometric calibration systems are used for the EMI. The
255 integrating sphere system with a tungsten halogen lamp is for the radiometric calibration of the UV2, VIS1, and VIS2 channels. Furthermore, the diffuser plate with a 1000 W xenon lamp (Newport Xenon-6269) is for the UV1 channel (240–315 nm), which produces a sufficient UV output. The radiance of the radiometric calibration system is monitored by a spectral radiometer, that is, Ocean Optics MAYP11868 (200–650 nm) for diffuser plate system and USB2000 (200–800 nm) for the
260 integrating sphere system. The EMI must rotate to complete the radiometric calibration because illuminating the entire 114 °instantaneously by the calibration system is infeasible.

The accuracy of the radiance directly determines the EMI radiometric calibration results. Therefore, the spectral radiometers must also be calibrated. Thus, an NIST-calibrated deuterium lamp (Newport) and a 1000 W FEL quartz tungsten halogen lamp (OSRAM) are selected to calibrate MAYP11868 and
265 USB2000, separately. The lamps illuminate a stand diffuser plate, which converts the lamp irradiance to radiance to calibrate the spectral radiometer, during calibration. The calibrated accuracy of the spectral radiometer is determined by three factors as follows: (1) accuracy of the lamp irradiance standard, (2) accuracy of converting irradiance to radiance, and (3) response accuracy of the spectral radiometer. These factors are discussed in detail below.
270 The accuracy of the lamp irradiance is traced to the NIST: the deuterium lamp irradiance at 50 cm is 3.16% in 210–350 nm, and the FEL quartz tungsten halogen lamp irradiances at 50 cm are 3.00%−2.40% in 250–400 nm and 2.40%−1.60% in 400–800 nm.

The method for converting irradiance to radiance is expressed as

$$L_{rad} = E_{lamp-irrad} \cdot (\frac{l_{lamp-plate}}{l_{50cm}})^2 \cdot BRDF_{std-plate}, \quad\quad\quad (3)$$

where L_{rad} is the radiance that is converted from the lamp irradiance $E_{lamp-irrad}$ at $l_{lamp-plate}$, which is

50 cm for the spectral radiometer calibration, that is, $l_{50cm} = 50cm$; and the stand diffuser plate

$BRDF_{std-plate}$ is close to $\frac{1}{\pi}(sr^{-1})$, with the accuracy of 1.25%. The distance between the stand diffuser

plate and the lamp is 500 ± 1 mm.

An optical fiber and a small telescope are used by spectral radiometer to observe the stand diffuser plate at an angle of 40°. A total of 100 measurements were obtained by the spectral radiometer. The accuracy of MAYP11868 response is less than 0.80%. The accuracy of USB2000 response is less than 0.50%. In practice, the radiance monitored by the spectral radiometer is usually different from the radiance of the diffuser plate. Therefore, the spectral radiometer needs to work in the linear response region. Five different radiance levels are observed by the spectral radiometer to determine the accuracy of the response linearity. The accuracy of MAYP11868 response linearity is less than 1.20%, and the accuracy of USB2000 response linearity is less than 1.10%.

Table 6. Calibrated accuracy of the spectral radiometer

Uncertainty/%	MAYP11868 (210nm-350nm)	USB2000 (250nm-400nm/400nm-800nm)
Lamp irradiance standard	3.16	3.00-2.40/2.40-1.60
Converting (Irradiance to radiance)	1.27	1.27
Spectral radiometer	1.44	1.21
Total	3.70	3.48-3.00/3.00%-2.38

For the diffuser plate radiometric calibration system, 1000W xenon lamp illuminates the same stand diffuser plate discussed above to produce a near-uniform surface light source, which is also produced at the integrating sphere opening by introducing the halogen tungsten lamp light to the sphere through a round pipe. The two radiometric calibration systems have their own highly stabilized power supply. The radiometric accuracy of the calibration system is shown in Table 7.

Table 7. Radiometric accuracy of the calibration system

Uncertainty/%	Diffuse plate system (210nm-350nm)	Integrating sphere (250nm-400nm/400nm-800nm)
Surface light source	< 2.00	< 2.00
Spectral radiometer	3.70	3.48-3.00/3.00-2.38
Total	< 4.21	< 4.02-3.61/3.61-3.11

295

3.2 Radiance calibration

The data N_{signal} collected by EMI including dark signal N_{dark} and light signal N_{light} is given by the following:

$$N_{signal} = N_{dark} + N_{light}, \tag{4}$$

300 where $N_{dark}, N_{light} \propto T_{time}, G_{gain}$, the integration time T_{time} can be set to 0.5, 1, and 2 s, the gain steps G_{gain} can be set from 0 to 63 with the interval of 1.

To obtain an approximate dark correction and to widely remove the dark-current-induced spectral structures, the mean dark spectra is subtracted [*Birgre Bohn et al., 2017*]. The dark and light signals are discussed separately below.

305 **Dark signal**

The e2v-CCD4720 and e2v-CCD5530 are adopted for the UV and VIS channel separately. As the weak UV band of the atmospheric light, the two UV channel CCDs are cooled to −20 ℃ to reduce the dark signal. The CCDs for the visible channels do not have independent temperature control, but they work in a constant temperature environment. The temperature is similar to that in the spectrometer, 310 which has temperature control. An investigation done after launch shows that the temperature stability is better than 0.1K over one orbit. This temperature variation over the orbit leads to very small change of the background signal.

Dark signal is obtained when no photons enter the instrument is to add the bias value (electronic offset) N_{bias} and the dark-current $N_{current}$ multiplied by the integration time t_{inte}.

315
$$N_{dark} = N_{bias} + N_{current} \cdot t_{inte} \tag{5}$$

The read-out register within the CCD has an excess of 16 blank pixels, which can be used to measure the electronic offset on the ground. The measurements show that the offset is not constant but drifts with time (about 0.5% /min). Therefore, the electronic offset is obtained per measurement frame in-orbit, and the electronic offset correction is implemented in the L1b data processor. The dark-current signal is a

320 thermally induced dark-current that increases with temperature and integration time [*Evelyn Jakel et al., 2007*]. Therefore, a dark signal measurement should be conducted frequently to update the dark data. The dark signal under different integration times is shown in Fig. 5 with UV2 and VIS1 channels as examples.

325
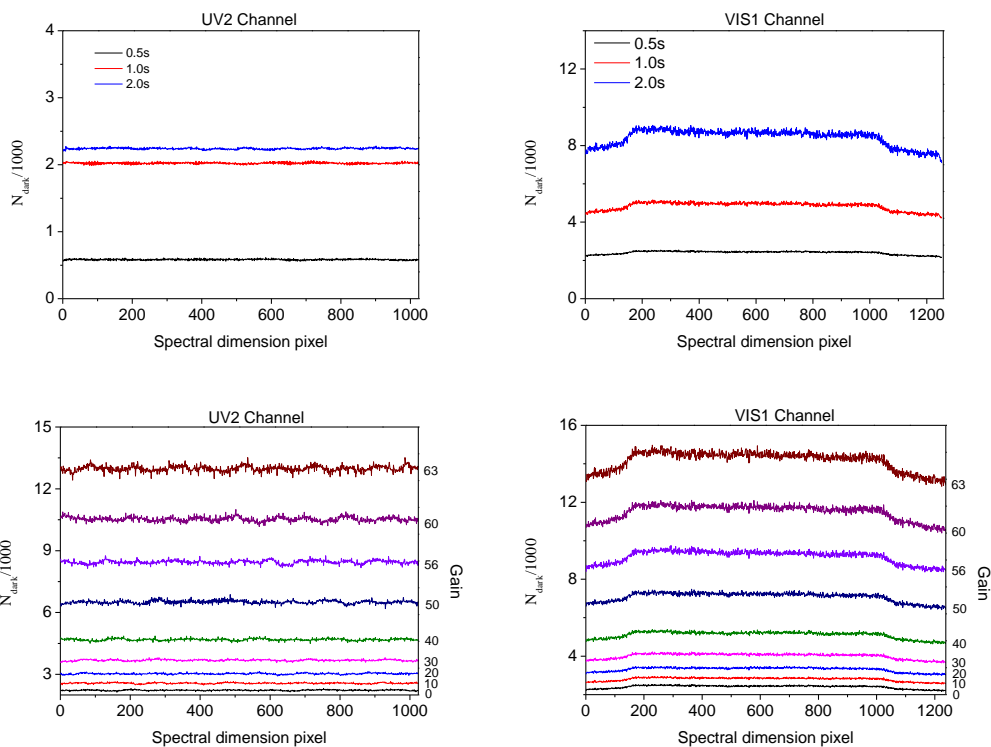
Fig.8. Top: Dark signal for different integration time. Bottom: Dark signal under different gain steps. The gain steps are set to 0, 10, 20, 30, 40, 50, 56, 60, and 63. The pixels in the readout register cannot be used to accomplish the binning due to the full well limitation. In this case, the pixel binning is
330 accomplished in the Field Programming Gate Array. Fast readout frequency is needed for the process. The fast readout frequency leads to signal distortion. Therefore, the difference between the measurements with 0.5 and 1.0 s integration times is not half of the difference between the measurements with 1.0 and 2.0 s integration times. Based on the signal distortion, we have obtained absolute radiance calibration key data at different integration time on the ground. The calibration key
335 data are used for the L1b data processor.

In Fig. 8, the small spectral structure in dark signal is caused by dark noise, which could influence the measured data, especially under weak-light conditions. The dark noise can be obtained by deriving standard deviations of repeated dark measurements and can be reduced by averaging the repeated dark. The dark spectra are recorded for each orbit when EMI is in orbit, and then, the dark spectra under the

340 same working conditions are averaged to correct the observation spectra.

Light signal

The radiometric calibration systems can provide different output-radiance levels. For UV1 channel, the EMI instrument views the standard diffuser plate at an angle of 45.0 ° and at a distance of 50.0 cm. Approximately 13 ° viewing angle of EMI can be illuminated once. Thus, the instrument has to be

345 rotated in nine steps to complete the entire 114 °. For the UV2, VIS1, and VIS2 channels, EMI views the integrating sphere opening at a distance of 40.0 cm, and approximately 11 ° can be illuminated once. A total of 11 steps are required to complete the radiance calibration.

The dark signal is firstly deducted from the radiance calibration data. One radiance level of the radiance calibration systems and the corresponding response of the EMI instrument are shown in Fig. 9.

350
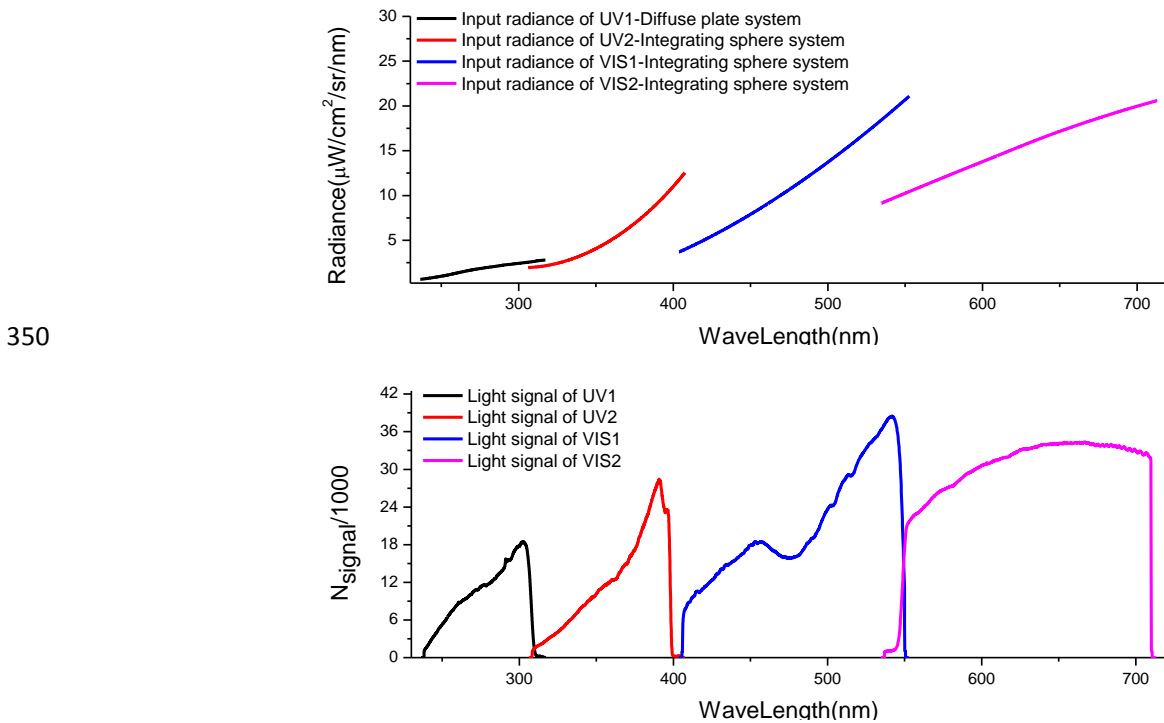
Fig.9. Upper panel presents one radiance level of the diffuser plate and integrating sphere system. The lower panel presents the EMI response to the radiance at integration times 2s (UV1), 1s (UV2, VIS1, VIS2), and at gain step 0. The dark signal is subtracted from the response.

355 Figure 9 illustrates an overlap band at each end of the channels, which is due to the optical features of the color separation filters. In addition, the response in the wavelength range 460–480 nm of VIS1 channel lowered, because a filter of this range is placed in front of Slit 11 to ensure that the detectors are unsaturated in the case of clouds.
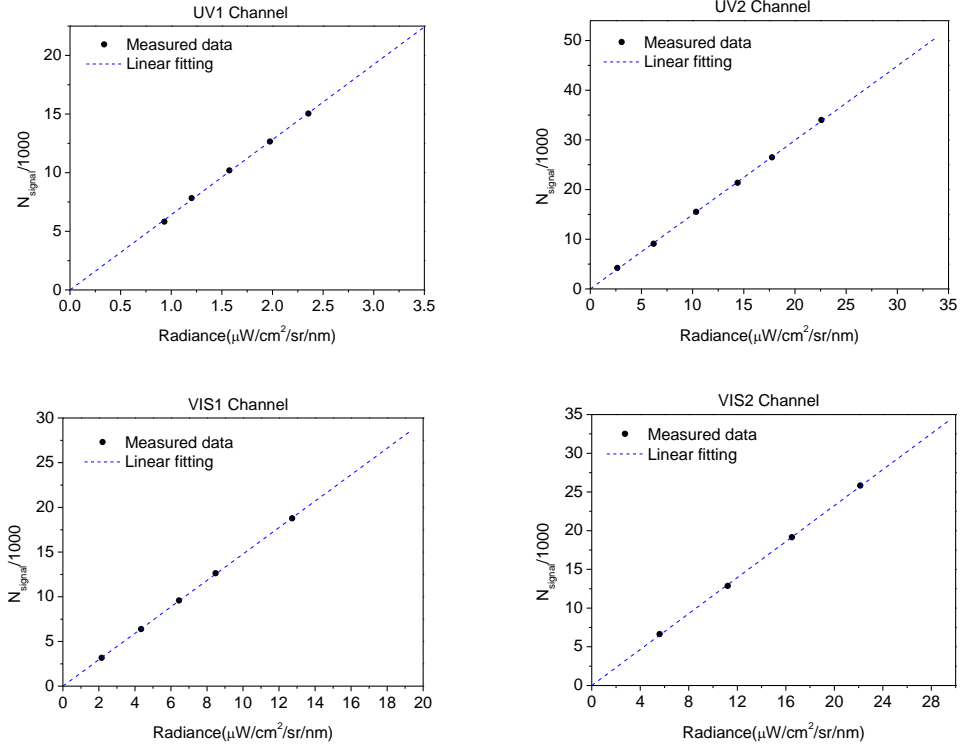
Fig.10. Linear response of the EMI, the signal is corrected by the dark signal. A non-linear response region exists under very low light signal (equal to the dark signal) condition and high light signal (saturation light signal) condition. The integration time, CCD readout, and gain steps are set up to ensure that the EMI works in the linear response region.

Base the linear response of the EMI, the radiance calibration model is as follows:

$$L_{radiance} = \alpha \cdot N_{Light}, \tag{6}$$

where $L_{radiance}$ is the radiance at the EMI entrance pupil, and α is the radiance response coefficient.

The theoretical relation between gain steps f_{gain} and gain value f_{magn} is determined using the following equation:

$$f_{magn} = \frac{5.8}{1 + 4.8 \cdot (63 - f_{gain})/63}. \tag{7}$$

The light signal under different gain steps is exhibited in Fig. 11, which uses the UV2 and VIS1 channels as examples.
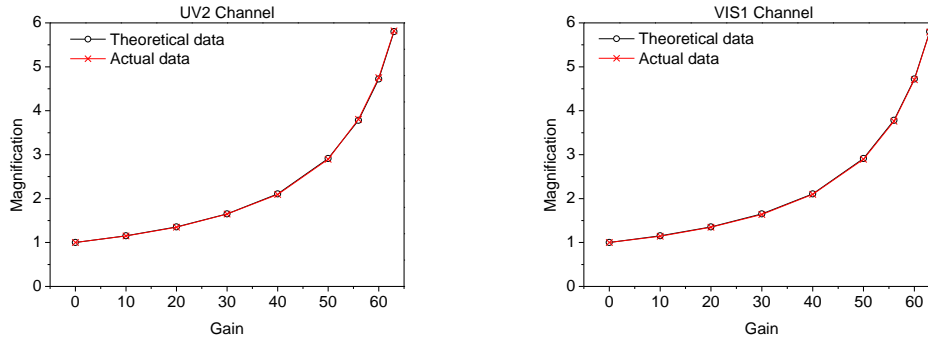
Fig.11. Relation between gain steps and gain value are presented. The relative deviation between theoretical and actual data is less than 1.0%. In application, the gain value can be obtained from the theoretical relation.

The overall accuracy of the radiance calibration is mainly determined by the accuracy of the radiance calibration system, by the response non-linearity, and by the accuracy of response of the EMI. The accuracy of the diffuser plate system and integrating system is shown in the Table 7. The response non-linearity can be calculated by the data in Fig. 8, and the results are as follows: 1.13% (UV1), 1.04% (UV2), 1.07% (VIS1), and 1.00% (VIS2). The response accuracy is obtained by 1000 repeated spectra of the EMI, and the results are 1.21% (UV1), 1.26% (UV2), 1.12% (VIS1), and 1.14% (VIS2). The accuracy of the conversion of different gain steps should be considered in the case of the light signal corrected by the gain value. The final accuracy of the radiance calibration is summarized in Table 8.

Table8. Radiance calibration accuracy

Channel	Accuracy(%)	
	No gain value corrected	Gain value corrected
UV1	4.53	4.64
UV2	4.52	4.63
VIS1	4.31	4.43
VIS2	4.30	4.42

The pre-flight, radiometric calibration of EMI was not conducted under flight-like vacuum and possibly under thermal conditions due to the limitation of the calibration facility. The EMI on-ground response to the quartz tungsten halogen WLS (6 V, 10 W) is displayed in Fig. 12, which uses UV2 and VIS1 as examples.

390
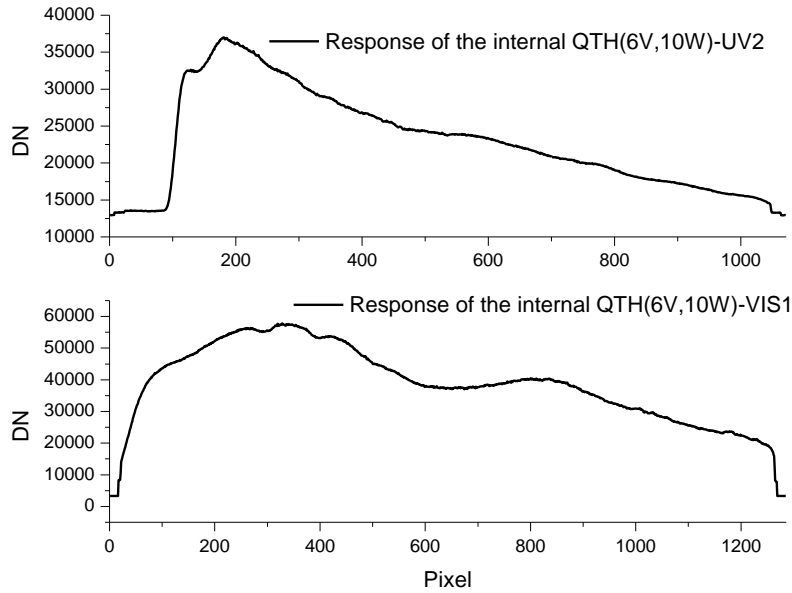
Fig.12. EMI on-ground response to the quartz tungsten halogen WLS

The EMI in-orbit response to the quartz tungsten halogen will be obtained after the launch. The change
between the on-ground and in-orbit responses is used to correct the preflight radiometric calibration,
which in turn is used to accomplish the in-flight absolute radiometric calibration of the flight data.

395 **3.3 Irradiance calibration**

The solar irradiance is calibrated mostly through the onboard diffusers [*S.Noel et al., 2006, Xiaoxiong Xiong
et al., 2009*]. The irradiance calibration depends on the incident angles on the onboard diffusers of the
EMI. The azimuth angle varies slowly throughout the year from about 16 ° to 28 ° around the nominal
value of 22 °. The elevation angle varies from +4 ° to −4 ° around the nominal value of 11 °. The elevation
400 angle change originates from the satellite orbital movement. Approximately 75 images are obtained
during a solar observation sequence of 150 s, and each individual image must be corrected for
radiometric goniometry.

$$DN_{\alpha_0,\beta_0} = DN_{\alpha,\beta} \cdot f_{\alpha,\beta}, \tag{8}$$

where DN_{α_0,β_0} is the image at the nominal azimuth angle α_0 and elevation angle β_0, which is

405 corrected from the $DN_{\alpha,\beta}$ with the goniometry correction factor $f_{\alpha,\beta}$. The corrected images are

averaged to improve the SNR. The irradiance calibration model of the EMI is as follows:

$$I_{Sun} = [\frac{1}{n}\sum_{i=1}^{n}(DN_{\alpha,\beta} \cdot f_{\alpha,\beta})_i] \cdot \sigma_{\alpha_0,\beta_0}, \tag{9}$$

where $n = 75$, $\sigma_{\alpha_0,\beta_0}$ is the irradiance response coefficient. The goniometry correction factor and

irradiance response coefficient of the EMI are calibrated on the ground. A light source has a beam
410   divergence comparable to that of the sun. This light source is rotated to cover the azimuth and elevation
angle ranges. The goniometry correction factors are shown in Fig. 13, which are by definition 1.00 for
the nominal azimuth and elevation angles.
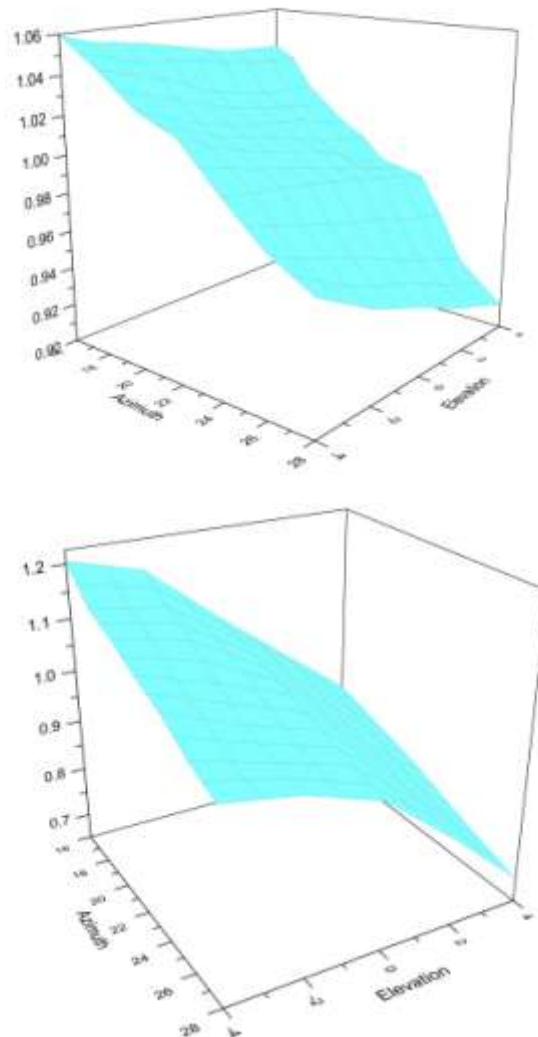
415   Fig.13. Goniometry correction factors for the aluminum diffuser (upper panel) and QVD (lower panel)

for the CFOV.

The NIST-calibrated 1000W FEL quartz tungsten halogen lamp is used for the absolute irradiance calibration at the nominal azimuth and elevation angles. The irradiance response coefficient $\sigma_{\alpha_0,\beta_0}$ is obtained for the irradiance calibration model of the EMI.

Aluminum diffusers adopted by the SCIAMACHY project introduce spectral structures in the sun reference spectrum [*C.E. Sioris et al., 2004*]. These structures are comparable to trace gas absorption features. They may interfere with DOAS-based retrieval of trace gases, thereby affecting the accuracy of the retrieved column densities [*A.Richter et al., 2001,2002, Courreges-Lacoste et al., 2004*]. As the QVD introduces considerably less structure than the aluminum diffuser, the EMI used it to provide the solar reference spectrum once per day. The aluminum diffuser is mainly used for radiometric calibration purpose, which is performed once a month.

The EMI works in low Earth orbit (LEO) at an orbit altitude of 708 km. The critical space environment will affect the performance of materials and components in LEO [*Samuel F. Pellicori,2014*], such as atomic oxygen (AO) [*Bruce A. Banks et al., 2008*], solar UV, and the energetic protons trapped in the inner Van Allen belt. Space radiation exposure effects on onboard diffusers have been tested and discussed in a previous study [*MinJie Zhao et al., 2015*].

4 Signal-to-noise ratio

The EMI is needed to meet the SNR requirements for dark scenes, especially in the UV bands [*Johan de Vries et al., 2009*], to ensure the accuracy of retrieved results. An SNR model is introduced, and it is in good agreement with the experimental result. The EMI in-orbit SNR is estimated by using the SNR model and MODTRAN [*A. Berk et al., 1989*]. The SNR estimation for advanced hyperspectral space instrument have been discussed elsewhere[*Andreas Eckardt et al., 2005, Lang Junwei et al., 2013*].

The electrons generated by a signal pixel can be calculated by the following:

$$s_e = \frac{\pi}{4}(\frac{D}{f})^2 \cdot \tau(\lambda) \cdot L(\lambda)\frac{A_d t_{int}\lambda}{hc}\eta(\lambda)\Delta\lambda \, , \tag{10}$$

where D/f is the relative aperture of optics, h is the Plank constant, c is the light speed, $\tau(\lambda)$ is the transmission of optics, $L(\lambda)$ is the sensor input radiance in $\mu W/cm^2/sr/nm$, $\Delta\lambda$ is the spectral bandwidth of a single spectral line, A_d is the pixel area, t_{int} is the integration time, and $\eta(\lambda)$ is the quantum efficiency of CCD.

The main part of the total noise is the shot/photon noise generated by the incident radiation. The

445 shot/photon noise can be described by the Poisson distribution, and can be calculated as follows:

$$\delta_{shot} = \sqrt{S_e} \; . \tag{11}$$

The other noises include a dark noise δ_{dark} and a readout noise of the CCD δ_{read}. Generally, the SNR can be calculated using the following equation:

$$SNR = \frac{S_e}{\sqrt{\delta_{shot}^2 + \delta_{dark}^2 + \delta_{read}^2}} \; . \tag{12}$$

450   The SNR can be improved by pixel binning,

$$SNR = MS_e / \sqrt{MS_e + M\delta_{dark}^2 + \sigma_{read}^2} \; , \tag{13}$$

where M is the binning factor (Table 1).

The output digital number of a signal pixel is obtained by the conversion factor f of the CCD:

$$DN = f \cdot S_e \tag{14}$$

455   For the SNR model of the EMI, it is impossible to measure the signal and noise separately. One way to do this in practice is to adopt the mean value of the repeat DNs as the signal and to adopt the standard deviation of the repeat DNs as the noise. In this case, N repeated measured spectra of EMI are recorded by observing the uniform-stable light source of the calibration system. The measured SNR is calculated by the following:

460
$$SNR = \frac{\overline{DN}}{\sqrt{\dfrac{\sum\limits_{i}^{N}(DN_i - \overline{DN})^2}{N\text{-}1}}} \tag{15}$$

The offset is deducted from the DNs. Fig. 14 shows the simulation and measured SNR results of VIS1 at the input sensor radiance.
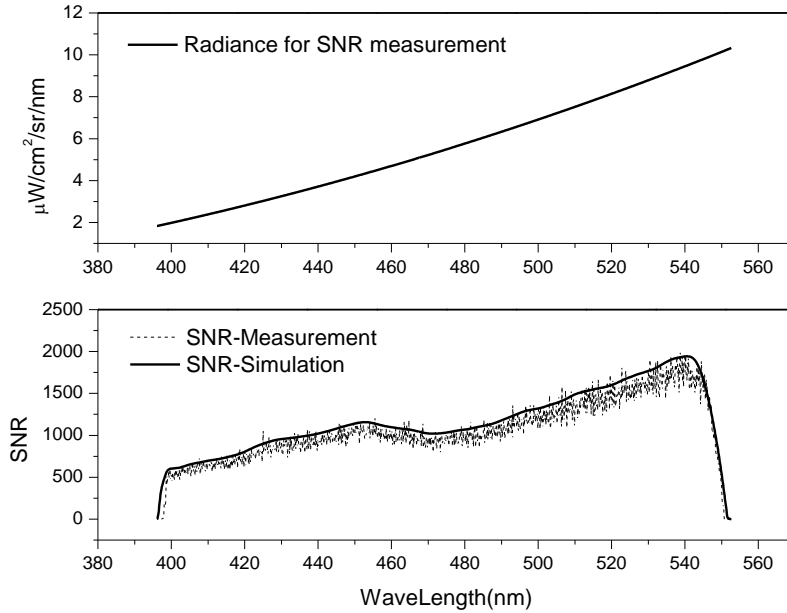
Fig.14. Upper panel presents the radiance of the integrating sphere system for SNR measurement of
VIS1 in the laboratory. The lower panel presents the results of measured SNR (solid line) and
simulation result (dotted line) for the radiance of the upper panel with an integration time of 2 s and a
binning factor of 4. The measured SNR in the wavelength range 460－500 nm lowers because a filter of
this range is placed in front of the slit 11 to make sure that the detectors are not saturated in the case of
clouds. There is an overlap band at the end of the channel, which is due to the optical features of the
color separation filter. In addition, there are 24 dark pixels at the end of the channel when the measured
SNR is approximately zero.

For the measured SNR, 100 repeated measured spectra of EMI are recorded by observing the
integrating sphere system with an integration time of 2 s. For the simulation SNR, the F-number of EMI
optics $F\#=3.2$, the spectral width of VIS1 $\Delta\lambda=0.12nm$, the area of a single pixel
$A_d=22.5\times22.5(um^2)$, the integration time $t_{int}=2s$, and the binning factor $M=4$. Figure 14

demonstrates that the measured SNR is lower than the simulation SNR. However, SNR is a good choice
for estimating the EMI in-orbit SNR using the SNR model.

The simulation of the EMI in-orbit SNR in the UV2, VIS1, and VIS2 channels are displayed in Fig.
15. The in-orbit SNR of this channel is not estimated as the solar light in the band of channel UV1 (240
－310 nm) is absorbed by the atmosphere.
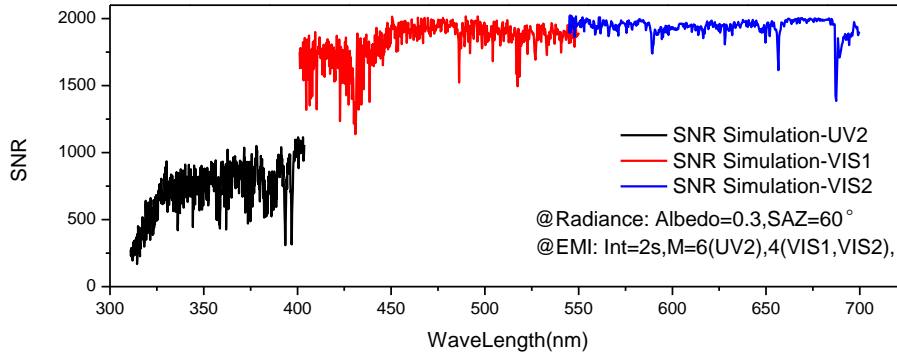
Fig.15. Simulation EMI in-orbit SNR of UV2, VIS1, and VIS2. The input radiance for the SNR model is obtained by MODTRAN with the albedo of 0.3 and with the sun zenith at 60 °. The EMI simulation SNR has an integration time of 2 s; it has binning factors of 6 for UV 2 channels and 4 for VIS channels. The spectral bandwidth of a pixel was 0.09 nm for UV2, 0.12 nm for VIS1, and 0.13 nm for VIS2.

The EMI in-orbit simulation $SNR_{simulation}$ is obtained by the radiance $R_{simulation}$ at an albedo of 0.3 and solar zenith of 60 °. The in-orbit simulation SNR at the radiance of 1.27/10.89 $\mu W / cm^2 / sr / nm$ can be achieved by the following equation:

$$SNR = SNR_{simulation} \cdot \sqrt{\frac{R}{R_{simulation}}} , \qquad (16)$$

where R is 1.27 for UV channels and 10.89 $\mu W / cm^2 / sr / nm$ for VIS channels.

For the in-orbit simulation SNR at the radiance of 1.27/10.89 $\mu W / cm^2 / sr / nm$, the results are presented in Table 9.

Table 9. In-orbit simulation SNR at the requirement radiance

Channel		SNR (simulation)	SNR (requirements)
UV2	330nm	328	200
	360nm	356	200
	390nm	388	200
VIS1	420nm	1860	1300
	480nm	1900	1300
	540nm	2040	1300
VIS2	560nm	2200	1300
	620nm	2300	1300
	680nm	2400	1300

5 Conclusions

The spectral and radiometric response performance of the EMI is obtained by preflight calibration. The on-ground calibration results are shown as follows:

Spectral calibration results:

UV1: 236.44–317.28 nm with the spectral resolution ≤0.45 nm;

UV2: 306.08–407.12 nm with the spectral resolution ≤0.49 nm;

VIS1: 395.50–552.63 nm with the spectral resolution ≤0.48 nm;

VIS2: 534.63–712.90 nm with the spectral resolution ≤0.49 nm;

The final accuracy of the wavelength calibration is <0.05 nm.

Radiometric calibration results:

UV1: 4.64%, UV2: 4.63%, VIS1: 4.43%, VIS2: 4.42%.

The on-ground calibration results meet the performance requirements of the EMI.

Simultaneously, the obtained calibration key data are used for the L1b processor. The EMI in-orbit performance after the launch may change given the vibration of the launching and changes in the environmental conditions. Therefore, the EMI in-orbit calibration is performed to verify preflight calibration and ensure calibration accuracy. For the EMI, the in-orbit wavelength calibration is performed by using the Fraunhofer lines in the solar and Earth spectra. The in-orbit radiometric calibration is performed by observing the sun through the onboard diffusers. During the EMI flight, the LEO space environment factors including AO, solar UV, and energetic protons will affect the EMI response performance. Aluminum diffuser and quartz tungsten halogen WLS are used to monitor the degradation of the EMI.

Acknowledgment

This research was supported by the National Natural Science Foundation of China (Grant No. 41705016).

References

520 A. Berk, L. S. Bernstein and D. C. Robertson, "MODTRAN: A Moderate Resolution Model for LOWTRAN7," Rpt. No. GL-TR-89-0122, Air Force Geophys. Lab., Bedford, MA 01731, 1-38, 1989.

Andreas Eckardt, Stefan Hofer, Christian Neumann, and Wolfgang skrbek. SNR estimation for advanced hyperspectral space instrument. Infrared Spaceborne Remote Sensing. Proceedings of
525 SPIE, 5883, 588303-1,2005.

A. Perez Albinana and R. Munro. The calibration of GOME-2 data. Infrared Spaceborne Remote Sensing X. Proceedings of SPIE 4818, 185-192, 2002.

A.Richter, T.Wagner.Diffuser plate spectral structures and their influence on GOME slant columns. Technical note, January 2001.

530 A.Richter, F.Wittrock.GOME MEASUREMENTS OF STRATOSPHERIC AND TROPOSPHERIC BrO. Adv Space Res. 29(11):1667-1672, 2002.

Birgre Bohn and Insa Lohse, Calibration and evaluation of CCD spectroradiometers for ground-based and airborne measurements of spectral actinic flux densities. Atoms. Meas. Tech., 10, 3151-3174, 2017.

535 B. Ording, A. Ludewig, R. Hoogeveen, D. ten Bloemendal, J. Dingjan, R. Voors, and J. de Vries. RESULTS OF THE TROPOMI CALIBRATION CAMPAIGN. International Conference on Space Optics-ICSO 2016. Proc of SPIE, 10562, 105623B-1, 2016.

Bruce A. Banks, Kim K. de Groh, Sharon K. Miller, and Deborah L. Watters, Lessons Learned From Atomic Oxygen Interaction With Spacecraft Materials in Low Earth Orbit,
540 NASA/TM-2008-215264.

C.E. Sioris, T.P. Kurosu,et al. Stratospheric and tropospheric NO2 observed by SCIAMACHY: first results. Advances in Space Research.34:780-785, 2004.

Courreges-Lacoste, Hedser van Brug, J.Groote Schaarsberg,et al. Spectral Features on reference diffusers: measurements and analysis. SPIE, 5234: 304-313, 2004.

545 Evelyn Jakel and Manfred Wendisch. A CCD spectroradiometer for ultraviolet actinic radiation measurements. JOURNAL OF ATMOSPHERIC AND OCEANIC TECHNOLOGY, 24, 449-462, 2007.

F. E. Nicodemus, J.C. Richmond, J. J. Hsia, I. W. Ginsberg, and T. Limperis, Geometric Consideration and Nomenclature for Reflectance, National Bureau of Standards, NBS monograph 160 Oct, 1977.

550 H. BOVENSMANN, J. P. BURROWS, M. BUCHWITZ, J. FRERICK, S. NOËL and V. V. ROZANOV, SCIAMACHY: Mission Objectives and Measurement Modes. JOURNAL OF THE ATMOSPHERIC SCIENCES. 56, 127-150, 1999.

Johan de Vries, Robert Voors, Ruud Dirksen and Marcel Dobber. In-orbit Performance of the Ozone Monitoring Instrument. Sensors, Systems, and Next-Generation Satellites IX. Proc. of SPIE, 5978,
555 59780T-1, 2005.

Johan de Vries, Robert Voors, Agnes Mika,et al.TROPOMI,the solar backscatter satellite instrument for air quality and climate, heads towards detailed design. SPIE, 7474:747409, 2009.

JOHN P. BURROWS, MARK WEBER, MICHAEL BUCHWITZ, VLADIMIR ROZANOV, ANNETTE LADSTÄTTER- WEI
β ENMAYER, ANDREAS RICHTER, RÜDIGER DEBEEK, RICARDA HOOGEN, KLAUS BRAMSTEDT, KAI-UWE
EICHMANN and MICHAEL EISINGER, The Global Ozone Monitoring Experiment(GOME): Mission
Concept and First Scientific Results, JOURNAL OF THE ATMOSPHERIC SCIENCES. 56,
151-175, 1999.

Kenneth J. Voss, Albert Chapin, Marco Monti and Hao Zhang, Instrument to measure the bidirectional
reflectance distribution function of surface, Appl. Opt. 39, 6197-6206, 2000.

Lang Junwei, Wang Yueming and Wang Jianyu. A new SNR Model for Space-borne Hyperspectral
Imagers Including Atmospheric Scattering Influence. International Symposium on Photoelectronic
Detection and Imaging 2013: Imaging Spectrometer Technologies and Applications. Proc. of SPIE,
8910, 891011-1, 2013.

Luis Guanter, Rudolf, Jose Moreno. Spectral calibration of hyperspectral imagery using atmospheric
absorption features. APPLIED OPTICS. 5(10):2360-2370, 2006.

Marcel Dobber, Ruud Dirksen, Pieternel Levelt, Gijsbertus ban den Oord and Quintus Kleipool,
EOS-Aura Ozone Monitoring Instrument in-flight performance and calibration, SPIE, 6296,
62960R-1- 62960R-12, 2006.

Minjie Zhao, Fuqi Si, Cheng Liu, Yihuai Lu, Yu Wang, Shimei Wang, Yi Zeng, Yu Jiang, Haijin Zhou,
Wenqing Liu. The effect of AO/UV/RD exposure on space-borne diffusers: A comparative
experiment. Appl. Opt. 54(31), 9157-9166,2015.

Pieternel F. Levelt, Gijsbertus H. J. van den Oord, Marcel R. Dobber, Anssi M äkki, Huib Visser, Johan
de Vries, Piet Stammes, Jens O. V. Lundell and Heikki Sarri. The Ozone Monitoring Instrument.
IEEE TRANSACTIONS AN GEOSCIENCE AND REMOTE SENSING. 44(5), 1093-1101, 2006.

P. S. Barry, J. Shepanski, C. Segal. Hyperion On-Orbit Validation of Spectral Calibration using
Atmospheric Lines and an On-board System. Proc. Of SPIE, 4480:231-235, 2002.

Quintus Kleipool, Antje Ludewig, Ljubisa Babic, Rolf Bartstra, Remco Braak, Werner Dierssen,
Pieter-Jan Dewitte, Pepijn Kenter, Robin Landzaat, Jonatan Leloux, Erwin Loots, Peter Meijering,
Emiel van der Plas, Nico Rozemeijer, Dinand Schepers, Daniel Schiavini, Joost Smeets, Giuseppe
Vacanti, Frank Vonk, and Pepijn Veefkind. Pre-launch calibration results of the TROPOMI payload
on-board the Sentinel 5 Precursor satellite. Atmos. Meas. Tech. Discuss. Discussion started: 13
February 2018.

Robert A. Neville, Lixin Sun, Karl Staenz. Detection of spectral line curvature in imaging spectrometer
data. SPIE, 5093:144-154, 2003.

Robert Voors, Johan de Vries, Ianjit S. Bhatti, Dan Lobb. TROPOMI, the Sentinel 5 precursor
instrument for air quality and climate observations: status of the current design. International
Conference on Space Optics-ICSO 2012.

Rosemary Munro, Rudiger Lang, Dieter Klaes, Gabriele Poli, Christian Retscher, Rasmus Lindstrot,
Roger Huckle, Antoine Lacan, Michael Grzegorske, Andriy Holdak, Alexander Kokhanovsky,
Jakob Livschitz, and Michael Eisinger. The GOME-2 instrument on the Metop series of satellites:
instrument design, calibration, and level 1 data processing-an overview. Atoms. Meas. Tech., 9,
1279-1301, 2016.

Ruud Dirksen, Marcel Dobber, Pieternel Levelt, Gijsbertus van den Oord, Glen Jaross, Matt
Kowalewski, George H. Mount, Don Heath, Ernest Hilsenrath and Johan de Vries, The on-ground

600   calibration of the Ozone Monitoring Instrument from a scientific point of view, SPIE, 5234, 400-410, 2004.

Samuel F. Pellicori, Carol L. Martinez, Paul Hausgen, and David Wilt, Development and testing of coatings for orbital space radiation environments, Appl. Opt. 53, A339-A350, 2014.

S.Noel, A.A.Kokhanovsky, O.Jourdan, et al. SCIAMACHY REFLECTANCE AND SOLAR
605   IRRADIANCE VALIDATION. Proceedings of the Third Workshop on the Atmospheric Chemistry Validation of Envisat. 2006.

Xiaoxiong Xiong, Junqiang Sun, Xiaobo Xie,et al. On-orbit Calibration and Performance of Aqua MODIS Reflective Solar Bands. IEEE TRANSACTIONS ON GEOSCIENCE AND REMOTE SENSING, 48(1):535-546, 2009.

610   Xuemin Jin and Robert Y. Levine, Bidirectional reflectance distribution function effects in ladar-based reflection tomography, Appl. Opt. 48, 4191-4200, 2009.